Earth and Planetary Science Letters 512 (2019) 59–70

Contents lists available at ScienceDirect

Earth and Planetary Science Letters

www.elsevier.com/locate/epsl

The origin of the transverse instability of aeolian megaripples

H. Yizhaq [a,*], G. Bel [a,b], S. Silvestro [c,d], T. Elperin [e], J.F. Kok [f], M. Cardinale [g], A. Provenzale [h], I. Katra [i]

[a] Department of Solar Energy and Environmental Physics, BIDR, Ben-Gurion University of the Negev, Sede Boqer Campus 8499000, Israel
[b] Center for Nonlinear Studies (CNLS), Los Alamos National Laboratory, Los Alamos, NM 87545, USA
[c] INAF Osservatorio Astronomico di Capodimonte, Via Moiariello 16, 80131 Napoli, Italy
[d] SETI Institute, Carl Sagan Center, 189 North Bernardo Avenue, Mountain View, CA 94043, USA
[e] Department of Mechanical Engineering, The Pearlstone Center for Aeronautical Engineering Studies, Ben-Gurion University of the Negev, P.O.B. 653, 8410501, Israel
[f] Department of Atmospheric and Oceanic Sciences, University of California, Los Angeles, CA 90095, USA
[g] Dipartimento di Scienze Psicologiche, della Salute e del Territorio, Università degli Studi G. d'Annunzio, Chieti, Italy
[h] Institute of Geosciences and Earth Resources, CNR, Pisa, Italy
[i] Department of Geography and Environmental Development, Ben-Gurion University of the Negev, Beer Sheva, 8410501, Israel

ARTICLE INFO

Article history:
Received 5 July 2018
Received in revised form 2 January 2019
Accepted 15 January 2019
Available online xxxx
Editor: A. Yin

Keywords:
megaripples
sand flux
saltation
reptation, transverse instability
wind tunnel
grain size analysis

ABSTRACT

Flat sand beds subjected to wind stress are unstable, and the wind action results in two types of aeolian sand ripples: normal ripples and megaripples. The distinction between the two types is based on two characteristics: i) the normal ripple pattern usually has a wavelength of up to 30 cm, while the megaripple wavelength is on the order of meters; and ii) unimodal distributions of sand grain size lead to normal ripples, while bimodal distributions result in megaripples. On Mars, the distinction between the two types is more difficult to ascertain because the length scales of normal ripples and megaripples can overlap, and often, there is no detailed information regarding their grain size distribution. Unlike normal ripples, megaripples show transverse instability, whose mechanism remains elusive, resulting in a much larger sinuosity of the crestline than normal ripples. In this study, we investigate the megaripples' transverse instability by using field measurements, wind tunnel experiments and numerical simulations of a three-dimensional ripple model. We show that (a) coarse grains accumulate at megaripple crests, with a corresponding reduction of the lateral sand transport along the crest, and (b) the transverse instability of megaripples is generated by a positive feedback between the height of the crest and the accumulation of coarse grains, with more grains accumulating on the higher portions of the crest. The outcomes of this positive feedback are that the thickness of the coarse grain armoring layer along the crest is not uniform and that it correlates with the crest height. In turn, these height differences drive the transverse instability such that higher portions of the ripple migrate more slowly than the lower sections, creating a wavy crestline. An analysis of Martian ripple images shows variations in the sinuosity index, suggesting that this characteristic can be useful in distinguishing between normal ripples and megaripples on Mars.

1. Introduction

Aeolian impact ripples, which form ordered patterns on sandy environments both on Earth and Mars, arise from the instability of flat sand surfaces under wind-induced transport of sand grains (Yizhaq et al., 2012a; Kok et al., 2012; Durán et al., 2014; Schmerler et al., 2016). Two different types of aeolian ripples, the so-called "normal" ripples and the megaripples (or granule ripples), are observed in nature (Bagnold, 1941; Sharp, 1963; Pye and Tsoar, 2009; Yizhaq et al., 2012a; Qian et al., 2012; de Silva et al., 2013; Yizhaq and Katra, 2015; Liu and Zimbelman, 2015; Foroutan and Zimbelman, 2016; Lämmel et al., 2018; Fig. 1 and Fig. S1). Normal ripples and megaripples have also been observed on Mars (Sullivan et al., 2005, 2008; Zimbelman et al., 2009; Zimbelman, 2010; Bridges et al., 2012; Zimbelman et al., 2013; Yizhaq and Katra, 2015, Silvestro et al., 2011; Vaz et al., 2017; Sullivan et al., 2018), where aeolian landforms are important

* Corresponding author.
E-mail addresses: yiyeh@bgu.ac.il (H. Yizhaq), bel@bgu.ac.il (G. Bel), silvestro@na.astro.it (S. Silvestro), elperin@bgu.ac.il (T. Elperin), jfkok@ucla.edu (J.F. Kok), marco.cardinale@unich.it (M. Cardinale), antonello.provenzale@cnr.it (A. Provenzale), katra@bgu.ac.il (I. Katra).

https://doi.org/10.1016/j.epsl.2019.01.025
0012-821X/

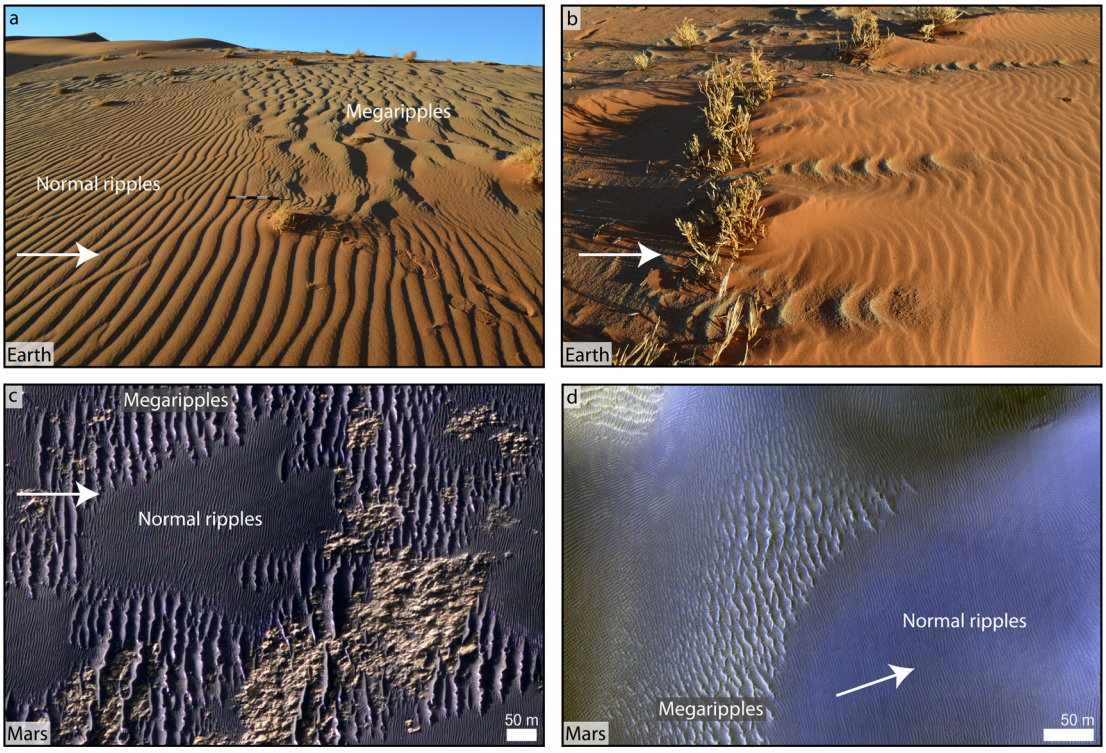

Fig. 1. Ripples on Earth and Mars. These different ripple types on both planets show different sinuosity values: whereas normal ripples are relatively straight, megaripple crests have a crescentic, barchanoid-like and irregular planform geometry. The arrows indicate the prevailing wind direction (see also Fig. S1). (a) A sharp transition between almost straight normal ripples (left) and wavy megaripples (right) on the downwind slope of a dune at Sossusvlei, Namibia (scale bar = 0.5 m). (b) Small coarse "barchan" megaripples formed between shrubs at Sossusvlei, Namibia, showing the main transverse instability pattern of megaripples. The coarse crescentic patterns are embedded in a background of straight normal ripples. (c) Normal ripples and megaripples in an unnamed crater in Noachis Terra (49.73°S, 11.36°E) (HiRISE image ESP_034801_1300). (d) Normal ripples and megaripples in Proctor Crater (47.79°S, 30.69°E) (HiRISE image ESP_011909_1320).

for understanding the planet's geology and atmospheric evolution (Rubin, 2006; Lapotre et al., 2016; Silvestro et al., 2016).

A bimodal mixture of grain sizes is needed for megaripple formation, in which coarse particles are more abundant at the crest (Yizhaq et al., 2009; Isenberg et al., 2011; Qian et al., 2012; Katra and Yizhaq, 2017). Megaripple growth starts with the coalescence of small ripples, resulting in the formation of larger ripples (Yizhaq et al., 2012a). Coarse and fine particles begin to segregate due to differences in their hop length. The coarse grains, which mainly move by creep and rolling, end up near the crest where the slope is very small. Eventually, the grain size distribution on the crest becomes bimodal, with an armoring layer of coarse grains covering the fine sand (Isenberg et al., 2011; Yizhaq et al., 2012a; McKenna Neuman and Bédard, 2016). This armoring layer allows the ripple growth to continue, since rare strong winds above the saltation threshold of the coarse grains are needed to destroy this layer (Yizhaq and Katra, 2015).

Observations of normal sand ripples indicate that they are effectively two-dimensional bedforms, displaying only small modulations in the direction transverse to the wind. In contrast, most megaripples have greater sinuosity due to the presence of a transverse instability, causing small undulations along the ripple crest to grow over time (Yizhaq et al., 2012b; Gillies et al., 2012; Fig. 1).

According to Rubin (2012), straight bedform crests or two-dimensional patterns arise in situations where along-crest coupling processes are strong enough to overcome the tendency toward three-dimensionality. For a ripple or a dune to have a straight, continuous crest, some physical mechanism must operate to couple the topography at different along-crest locations and to overcome local perturbations driven by natural heterogeneity in the system. Without such coupling, different points along the crest will not remain locked in phase but will be free to form breaks, bends, or junctions. Hypothetically, if the flow and topography along every streamline were completely decoupled from adjacent streamlines, "bedform" crests would be randomly phased from one streamline to another, and coherent bedforms could not exist, as in current ripples and fluid drag ripples (Bagnold, 1941; Lapotre et al., 2016). Rubin (2012) suggested three possible mechanisms for obtaining straight bedforms with unidirectional flow: along-crest flow, gravitational transport along an inclined crest, and ballistic splash. In his work, Rubin (2012) also suggested a mechanism that may contribute to 3D bedforms: "sorting of sediment by grain size into patches of sediment that respond differently to flow." This unexplored mechanism is the main focus of this work. In our previous work on the transverse instability of megaripples (Yizhaq et al., 2012b), we showed that megaripples are laterally unstable, and this instability was explained through the differences in the drift velocities of ripple sections along the crest, which differ in their heights. Without using any detailed modeling or experimental work, we suggested that non-uniform megaripple heights may develop due to irregularities in the accumulation of coarse particles. Here we used wind tunnel experiments, field measurements and a new mathematical modeling approach to explain the origin of the transverse instability of megaripples in detail and to show its relevance to the study of Martian bedforms.

In particular, we focus on the mechanism behind the megaripple transverse instability, and we show that it develops due to the presence of coarse particles at the ripple crest. Differences in the sinuosity between normal ripples and megaripples are due to non-uniform coarse grain accumulations along the crest, which are the result of a positive feedback between the surface coverage of coarse grains and ripple height. The resulting small lateral flux is not sufficient to inhibit the presence of irregularities along the

crest. Accumulations of coarse particles allow further growth of the ripples at these points, thus decreasing their migration rate and enabling further accumulation of coarse grains. This mechanism leads to variations in the thickness of the armoring layer along the ripple crest, which positively correlates with ripple height (illustrated schematically in Fig. S2). The new mechanism suggested here also explains why normal ripples, composed only of fine sand with no armoring layer of coarser grains, tend to be straight.

It is important to emphasize here that although transverse dunes are known to be laterally unstable due to different migration rates induced by differences in height along the cross-wind direction (Parteli et al., 2011), the exact mechanism is different from that of megaripples. According to the model of Parteli et al. (2011), the instability is due to lateral transport induced by gravitational downslope forces, which arise in areas where the local slope exceeds the angle of repose. This type of sand flux almost never occurs in megaripples where the splash mechanism dominates the sand transport and the lee slope is below the angle of repose (Sharp, 1963). In the dune model, the transverse instability is explained by a lateral flux from the smaller slice to the adjacent large slices, thus resulting in the growth of small perturbations (Parteli et al., 2011). In contrast, in megaripples, there is a smaller lateral reptation flux between the adjacent slices along the crest; thus, a larger slice accumulates more coarse particles that further increase its height and enhance the differences in migration rates. Despite the fact that for both dunes and megaripples, the transverse instability is due to different migration rates of peaks and troughs along the crest, the mechanisms are different. For dunes, it is the gravitational flux, whereas for megaripples, it is the smaller lateral reptation flux. The role of the coarse particles in megaripples is crucial; without them, only straight normal ripples would develop as shown in Fig. 1a.

A main consequence of the transverse instability of megaripples is their higher sinuosity index SI (Yizhaq et al., 2012a, 2012b; e.g., SI = 1.19 for the megaripple in Fig. S3), defined as the ratio between the real length of the crestline and the Euclidean distance (straight line) between the bedforms' end points. Because this characteristic can be easily derived from remote sensing images, it can be used to distinguish between normal ripples and megaripples on Mars, where in situ measurements are limited and remote images from orbiters are the main data sources (Bourke et al., 2010; Bridges et al., 2013; Cardinale et al., 2016; Hugenholtz et al., 2017).

2. Methods

The study includes grain size analyses (GSAs) of samples taken from megaripple crests in different locations, controlled wind tunnel experiments for measuring reptation flux, and numerical simulations of a mathematical model for aeolian sand ripples. In addition, we investigate the sinuosity index of Martian ripple images.

2.1. Field measurements

Sand samples were collected along megaripple crests from three sites: Nahal Kasuy (Yizhaq et al., 2012a) and Qetura Sands (Yizhaq and Katra, 2015) in the southern Negev Desert, Israel, and Wadi Rum in southern Jordan. Samples of sand were collected by pressing a tin can (diameter 84 mm, height 35 mm) (Yizhaq et al., 2009) into the ripple crest. The average sample weight was 310 g (with values ranging from 282 to 336 g).

The grain size distributions (GSDs) of the sand samples were analyzed by a high-resolution laser diffractometer technique (ANALYSETTE 22 MicroTec Plus) located at Ben-Gurion University over the range of 0.08 to 2000 μm with a resolution of 102 measuring bins with increasing size from 1 μm in the very fine fraction (clay) to 182 μm in the very coarse fraction. The samples were dispersed in a Na-hexametaphosphate solution (0.5%) by sonication (at 38 kHz), and then transferred to a fluid module of the instrument (containing deionized water). The data were processed using the Mie scattering model (refraction index = 1.56, absorption coefficient = 0.1). The MasControl software was employed to statistically determine the mean size, median, sorting values, modes, and size fraction weight in multiple modal distributions.

We measured the height and sinuosity of megaripples at the three study sites. The ripple heights were measured by a meter along the crest with 15-cm intervals by using the area between two ripples as the reference point (height = 0 cm). The sinuosity index was calculated as the ratio between the length of the line that follows the ripple crest (by an interval of 15 cm) and the length of the straight line that connects the two end points of the ripple crest (measured by a measuring tape).

2.2. Wind tunnel experiments

We conducted several experiments in the wind tunnel to study the mechanism of transverse instability under controlled conditions. In the first set of experiments, we used reptation traps (with a cross-section of 1 cm × 2 cm) to measure the sand mass flux along the wind direction (denoted by W) and in the lateral direction (denoted by L) with sand collected from Nahal Kasuy, characterized by a bimodal distribution that is typical of moderate-sized megaripples (748 μm coarse mode and 222 μm fine mode; Yizhaq et al., 2012a). In similar experiments, we measured the ratio L/W for almost unimodal sand (from 247–300 μm). The experiments were conducted in the stationary boundary layer tunnel of the Aeolian Simulation Laboratory at Ben-Gurion University (BGU), Israel. The BGU wind tunnel complies with aerodynamic requirements, and it is representative of common wind speeds (up to 25 m/s) (Pye and Tsoar, 2009; Katra et al., 2014). It is an open circuit tunnel that is composed of three parts: the entrance cone, the test section and the diffuser. A feeder is located close to the entrance cone to allow sand supply during the experiments. Air is sucked in through the bell-shaped entrance by a fan located at the end of the diffuser. The cross-sectional area is 0.7 × 0.7 m, and the working length for measurements in the test section is 7 m (Schmerler et al., 2016).

2.3. Martian ripple analysis

We mapped the ripples ($n = 4348$, n is the number of ripples) on one High Resolution Imaging Science Experiment (HiRISE) image from an unnamed crater of 80 km in diameter in the Noachis Terra region on Mars (49.7°S, 1.4°E) (Fig. 2). The study site was chosen because two classes of bedforms, ∼3-m-spaced ripples and ∼18-m-spaced megaripples, can be easily distinguished upwind from a field of dark-toned dunes (Fig. 2a). We chose the mapping sites by drawing three 700 × 700 m squares around randomly generated points from the rippled area in ArcGIS (Fig. 2a). We then computed and compared the sinuosity index distributions for the two ripple classes by manually digitizing the ripple crestlines on the 50 cm/pixel HiRISE and by computing their sinuosity in ArcGIS (Figs. 8b, c, S7 and S8). Mapping was performed at the scale of 1:400 for megaripples and 1:200 for ripples, which is sufficient to resolve the bedform crests. However, it should be noted that the sinuosity results are probably underestimated due to image resolution constraints. Despite this limitation, the sinuosity values are comparable to terrestrial values, thereby supporting the mapping performed in this study.

2.4. Numerical simulations

To study the effect of the lateral flux on ripple patterns, we used an extension of a 3D ripple model (Yizhaq et al., 2004) de-

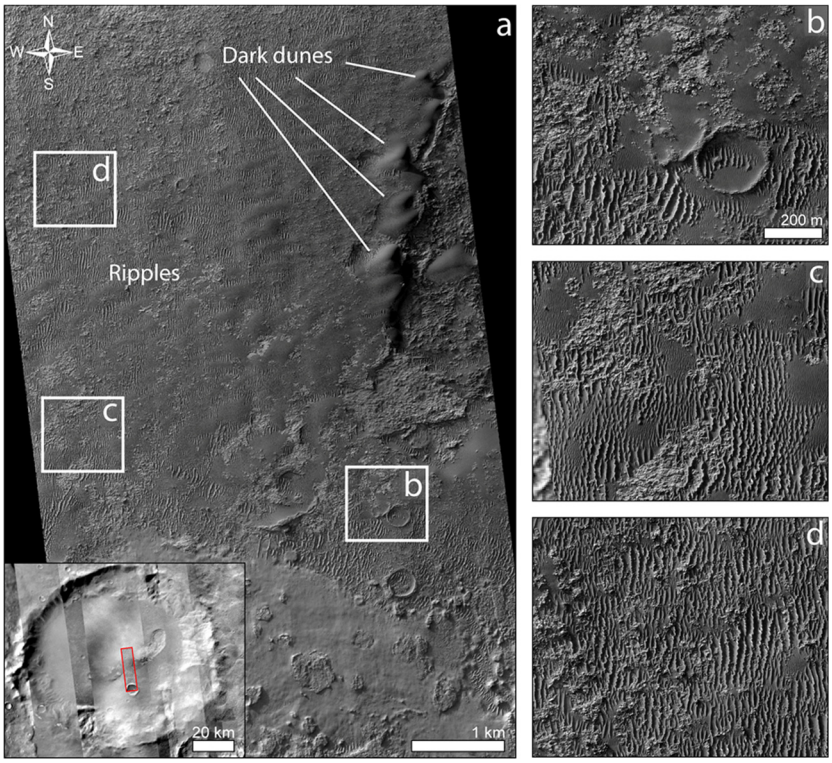

Fig. 2. Martian ripples examined in this study. (a) Location map of the study sites and footprint of HiRISE studied in this work (ESP_034801_1300, NASA/JPL/U of A). (b)–(d) Ripples mapped in this study.

veloped for normal sand ripples. The model is based on Anderson's idea (Anderson, 1987) that ripples develop due to spatial differences in the reptation flux and that the role of saltation is merely to introduce energy into the system. The lateral divergence of the flux is modeled by a diffusion term, $\mu z_{YY}\tan\varphi$ (z is the ripple height), whose intensity is quantified by a diffusivity parameter, μ, which depends on the grain size, and φ is the average impact angle of the splashing-saltating grains (measured from the horizontal surface; see Fig. 2 in Yizhaq et al., 2004). Small values of μ represent coarse particles (low lateral flux) while finer particles are associated with larger values of μ. μ represents the change in the reptation flux, Q_r, due to the slope that can be written as $Q_r = (1-\mu z_x)Q_r^0$ where Q_r^0 is the reptation flux on a flat bed (Yizhaq et al., 2004). Physically, part of the energy of the saltating grain is imparted to individual surface grains, which vibrate rapidly, and as a result can roll or slide down the slope (Isenberg et al., 2011). Hardisty and Whitehouse (1988) termed this mechanism an "impact-induced gravity flow," which acts to reduce the flux on the windward slope and to increase it on the lee face. This effect is more significant for fine grains due to their smaller mass. The 3D equation was developed through a long-wave approximation of the integro-differential equation of the full system (see Yizhaq et al., 2004 for more details) leading to the following dimensionless equation:

$$\begin{aligned} z(X,Y,T)_T = &-(1-\mu\tan\varphi)z_{XX} + \mu\tan\varphi z_{YY} \\ &+ \frac{\varepsilon}{2}\left[\overline{a^2}z_{XXX} + (\tan\varphi + 2\mu)\left(z_X^2\right)_X\right] \\ &+ \frac{\varepsilon^2}{2}\left[-\frac{\overline{a^3}}{3}z_{XXXX} + \left(z_X^3\right)_X - \frac{\overline{a^2}\tan\varphi}{2}\left(z_X^2\right)_{XX}\right] \end{aligned} \tag{1}$$

where z is the dimensionless ripple height, X and Y are along-wind and cross-wind directions, respectively, T is time, φ is the average impact angle (10° in the simulations, Kok et al., 2012), and a is the dimensionless reptation length of fine grains assumed as a random variable with a prescribed distribution (Yizhaq et al., 2004). The overbars denote averages over the probability distribution of a, and $\bar{a} = 1$ was used in the simulations. In the above equations, ε is a perturbation parameter, which measures the average nonlinearity (height over wavelength) of the ripples. As mentioned above, μ measures the strength of the sand flux along the Y direction, which is responsible for the lateral coupling (if $\mu = 0$, there is no coupling along the Y direction).

In order to model the feedback between the ripple height and the lateral flux, we used the following height dependence of μ, which now becomes space-dependent:

$$\mu(X,Y) = \mu_0\left(1 - \eta\tanh\left(\frac{z-\bar{z}_y}{\bar{z}_y}\right)\right) \tag{2}$$

where $\bar{z}_y(X) = \frac{1}{N}\sum_{i=1}^{N} z(X,Y_i)$ is the average height along the lateral direction for a given value of X. Thus, μ will be small for locations along the crest that are higher than the average, leading to a reduced lateral flux. The parameter $0 \le \eta \le 1$ dictates the strength of the feedback, and μ_0 is the value of μ without the feedback ($\eta = 0$, no height dependence of μ i.e. $\mu(X,Y) = \mu_0$). This form indirectly expresses the relation between the ripple height and the coarse fraction, and it was used to test whether small accumulations of coarse particles (associated with $\mu < \mu_0$) will continue to grow and initiate the transverse instability.

Eq. (1) was integrated using a fourth-order finite difference scheme for the spatial derivatives and a second-order Adams–Bashforth method for the time integration. A 512 × 512 grid was used, with periodic boundary conditions. The spatial resolution was 0.0307, and the time step was $2\cdot 10^{-6}$ (both space and time are dimensionless).

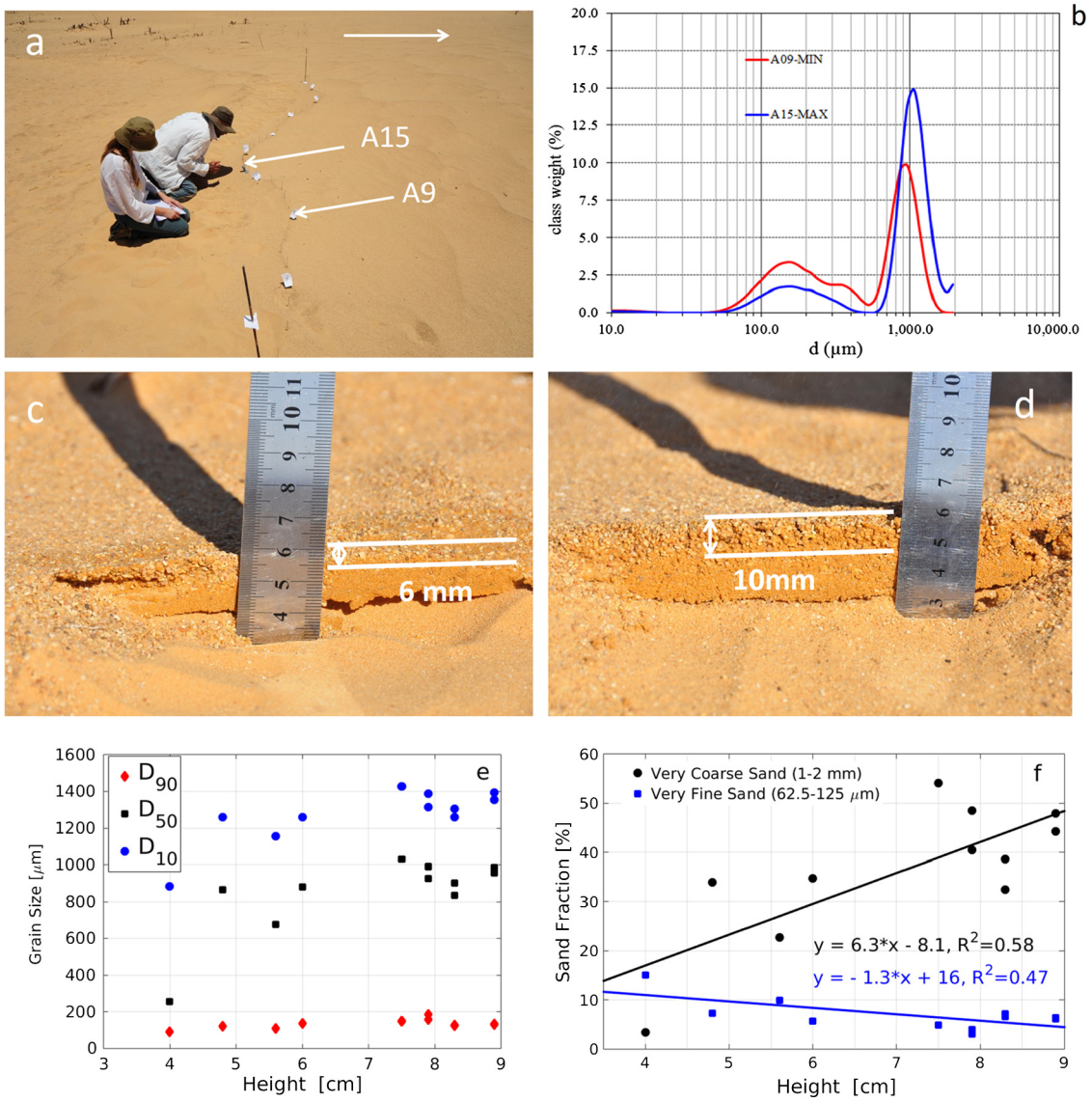

Fig. 3. The thickness of the armoring layer at a megaripple crest in Nahal Kasuy in the southern Negev Desert, Israel (the megaripple sinuosity is 1.12). (a) The locations where the crest was sampled are indicated by white arrows; point A9 is in the lower part of the crest, and A15 is at the highest point along the crest. (b) The GSAs of the two samples show that the grain size at A15 is much coarser than at A9. Cross-sections at these two points (panels c and d) show that the armoring layer at A15 (10 mm) is thicker than that at A9 (6 mm). (e) Grain size segregation versus ripple height for the megaripple shown in (a). The three measures increase with ripple height although this is more significant for D_{10}, which indicates the very coarse mode of the distribution. (f) The coarse fraction grows almost linearly with ripple height ($R^2 = 0.58$), whereas there is a less significant decrease in the very fine fraction ($R^2 = 0.47$).

3. Results

3.1. Field measurements

An important new observation for understanding the transverse instability of megaripples is that the thickness of the armoring layer along the crest is not uniform. Fig. 3 shows the results of grain size sampling along the crest of one megaripple at the Nahal Kasuy site (for more details on the site, see Isenberg et al., 2011). There is a significant difference in the thickness of the armoring layer between the point of maximum height along the crest (denoted as A15; 10 mm) and the point of minimum height (denoted by A9; 6 mm). The difference is also expressed in the GSDs of the samples taken from these locations. The GSDs are bimodal distributions that include the fine sand beneath the armoring layer. There are coarser grains at A15, compared with those at A9, expressed also in a coarser mode (1115 μm at A15 compared with 1010 μm at A9).

The cumulative percentile values, D_{10} and D_{90}, and the median D_{50} (the grain sizes at which 10, 90, and 50% of the grains are coarser, respectively, Blot and Pye, 2001) of samples taken along the megaripple crest versus the crest height are shown in Fig. 3e. The median and D_{10} increase with ripple height, such that the higher the crest, the coarser is the average grain size. Fig. 3f shows that the very coarse fraction (1–2 mm) increases linearly with ripple height, whereas the very fine fraction (62.5–125 μm) decreases (although less significantly) with ripple height. In the supplementary material (Figs. S3–S5), we show results of megaripples from different study sites. The general pattern is the same: the armoring layer thickness along the crest is not uniform, and it correlates with the ripple's height (see also Katra and Yizhaq, 2017).

This non-uniform grain size distribution along the crest, coupled with the small lateral flux, causes the differences in height along the crest to persist for long time periods. These differences may even become more evident, since more coarse particles driven by the impinging saltating grains accumulate at these points of the

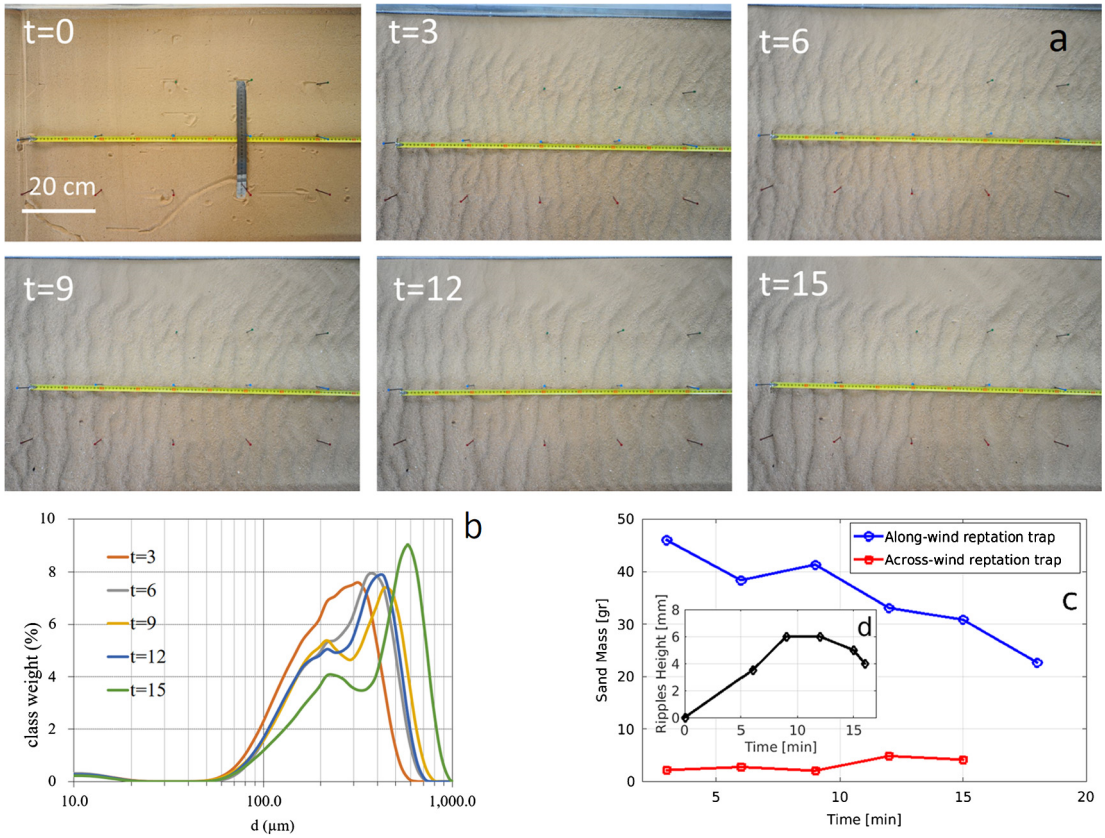

Fig. 4. (a) Time evolution of incipient megaripples in the wind tunnel starting from a flat bed (wind speed 7 m/s) with natural sand collected from Nahal Kasuy (time measured in minutes). (b) Grain size distribution of samples collected from the crest during ripple growth, showing the evolution of segregation. (c) The blue and red curves show the mass of reptating sand collected in the parallel and transverse directions with respect to the wind. The mass in the trap along the wind direction is at least four times larger than that in the cross-wind direction. The inset (d) shows the ripple height (in mm) during the experiment.

ripple, which migrate more slowly. Thus, under the influence of unidirectional winds, the basic mechanism of the transverse instability is a differential migration along the crest, which will increase the megaripple sinuosity as shown in Fig. S2.

3.2. Wind tunnel experiments

We conducted several experiments in the wind tunnel to study the mechanism of transverse instability under controlled conditions. Fig. 4a shows snapshots of the growth of small megaripples from a flat bed, and Fig. 4b shows the sorting process at the crest during the ripples' evolution. The initial bulk unimodal grain size distribution develops into a bimodal distribution, which is a fingerprint of megaripples (Lämmel et al., 2018). This sorting process happens for a wind speed that is above the threshold for the fine grains but below the threshold of the coarse grains. After 15 min of 7 m/s wind speed starting from a flat bed, the ratio of L/W (the ratio between along- and across-wind reptation flux) was around 0.16, whereas at the beginning, it was 0.06 (Fig. 4c). In similar experiments with almost unimodal sand (247–300 μm), the ratio of L/W was larger, approximately 0.5 ± 0.22. The smaller L/W ratio in the case of bimodal sand indicates that the lateral coupling in megaripples, where coarse grains cover the crest, is smaller than in unimodal sand ripples. This result fully supports our main hypothesis for the origin of the transverse instability of megaripples.

3.3. Numerical simulations

Fig. 5 shows results for different values of μ_0 in the absence of the feedback between the ripple height and the lateral flux ($\eta = 0$). For smaller values of μ_0, the ripples look wavier and discontinuous, similar to megaripples, whereas for $\mu_0 = 0.8$ (large lateral flux, i.e., fine sand grains within this modeling approach), the ripples are straight and continuous. Fig. 6 shows the sinuosity index (SI) and the roughness as a function of μ_0 for five realizations. Both measures (SI and roughness) decrease with μ_0 as in the case of normal ripples composed of fine sand.

Fig. 7 shows model simulations with the feedback defined in Eq. (2), starting from small perturbations superimposed at the crest onto one of the ripples in the center. These small perturbations drive the transverse instability, and as a result, the ripple sinuosity increases in time. Interestingly, the sinuosity or the perturbation moves forward to the downwind ripples, which are coupled by the diffusion term. For smaller values of η, the effect of the perturbations is smaller, as shown in Fig. 8. Fig. S6 shows that a similar phenomenon occurs for ripples in the field.

These numerical simulations support the idea that owing to the small lateral flux, initial accumulations of coarse particles at the ripple crest can grow in time, increasing the irregularities along the ripple crest and, consequently, increasing the ripple sinuosity.

3.4. Martian ripples

In Figs. 9a, 9b, S7 and S8, we show the variation in the sinuosity index of the Martian ripples. Most of the megaripples mapped in blue in Fig. 9a show higher sinuosity values than the normal ripples mapped in red. This is highlighted in the histogram in Fig. 8c. Normal ripples ($n = 3111$) reside in a lower sinuosity range (1 to 1.2) with a higher proportion of low sinuosity counts. Conversely,

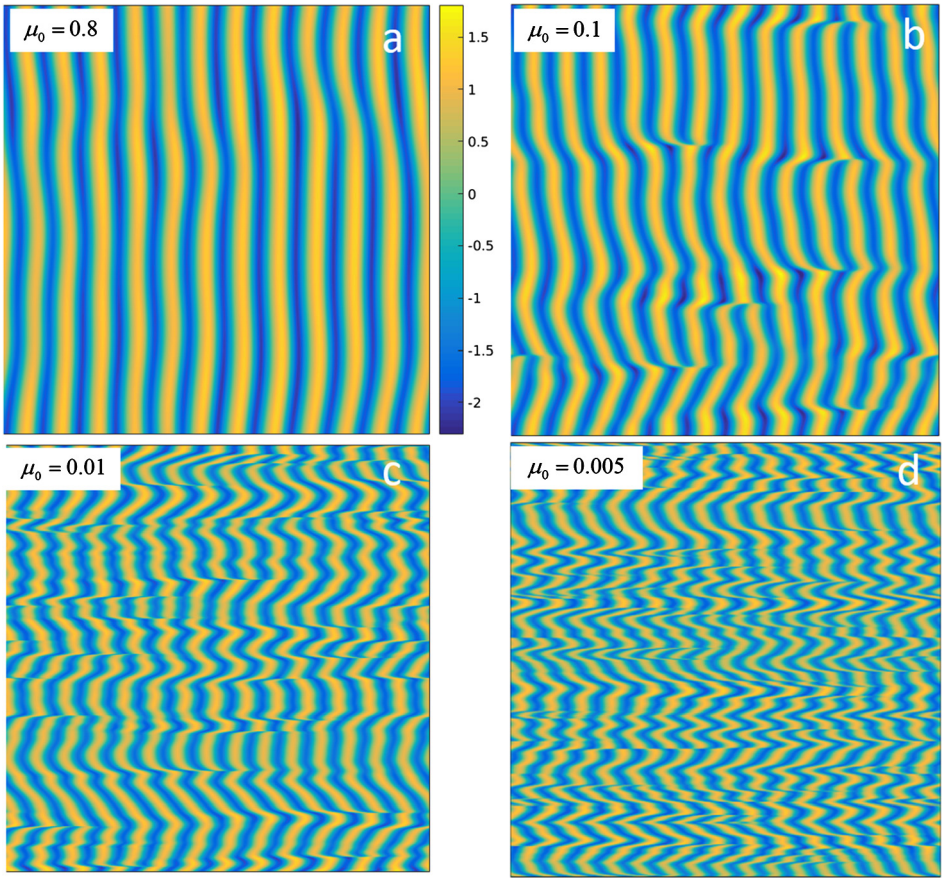

Fig. 5. 3D simulated ripples based on the Yizhaq et al. (2004) model, initiated from random initial conditions for different values of μ_0 (the parameter that controls the intensity of lateral flux) and with $\eta = 0$. The simulation time is the same in all the panels. For a smaller value of μ_0, the ripples look wavy and discontinuous due to the smaller lateral flux.

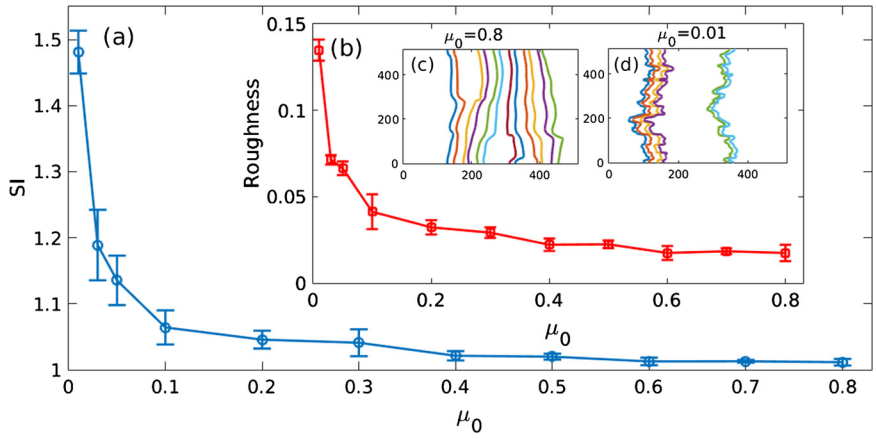

Fig. 6. The sinuosity index SI (a) and the roughness, the average magnitude of the deviation from the mean height (b) as a function of μ_0 calculated from five realizations of the model with $\eta = 0$. The insets (c) and (d) show typical contour lines for $\mu_0 = 0.8$ and $\mu_0 = 0.01$. Both measures (SI and roughness) decrease with μ_0, indicating that the ripples become more straight for larger cross-ripple coupling.

the megaripple sinuosity distribution ($n = 1234$) is wider with values ranging from 1.01 to 1.58. Below the third bin (sinuosity index = 1.042) of the histogram, there is a higher proportion of normal ripples, while megaripples dominate above this value. Important statistical parameters for the two distributions are summarized in the Supplementary Table 1. These results show a clear difference in the sinuosity index between normal ripples and megaripples, suggesting that, together with the wavelength, the sinuosity can be used to discriminate between these two bedform classes.

4. Discussion and conclusions

In this work, we propose a new mechanism to explain the transverse instability of megaripples. This mechanism is based on the feedback between the accumulation of coarse particles at the crest, the ripple height and the slower drift speed of the higher segments of the ripple. Due to the accumulation of coarser grains coming from the windward slope, whereas saltating fine particles hop over the crest, the higher segments along the crest become covered with a thicker armoring layer. These larger grains have

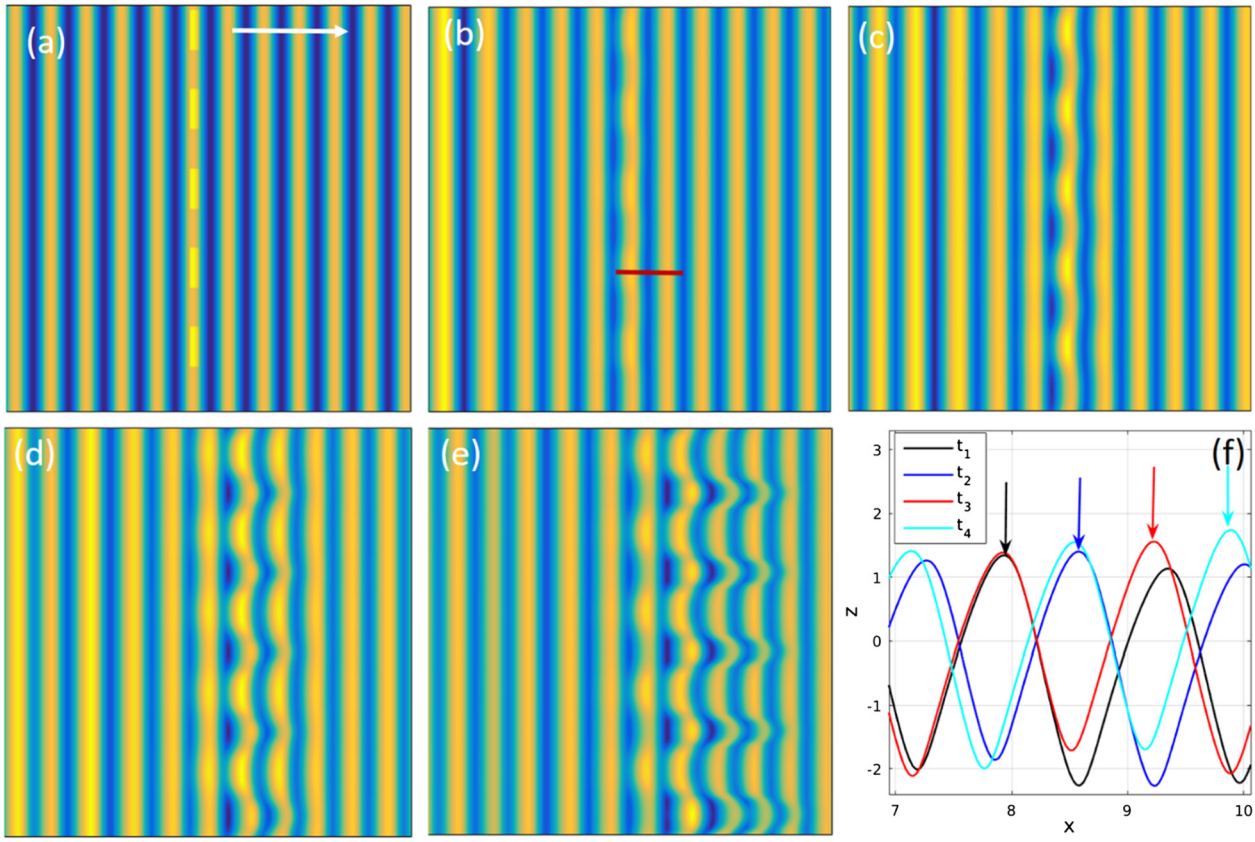

Fig. 7. Development of the transverse instability of simulated ripples from initial perturbations on one ripple in the center. Note how the lateral perturbations also move to the downwind ripples (see Fig. S10). Parameters: $\mu_0 = 0.8$, $\eta = 1$. The white arrow indicates the wind direction. Panel (f) shows the ripple cross-sections (across the red line in (b)) at different times. The ripple height increases over time due to the feedback between the height and the lateral flux.

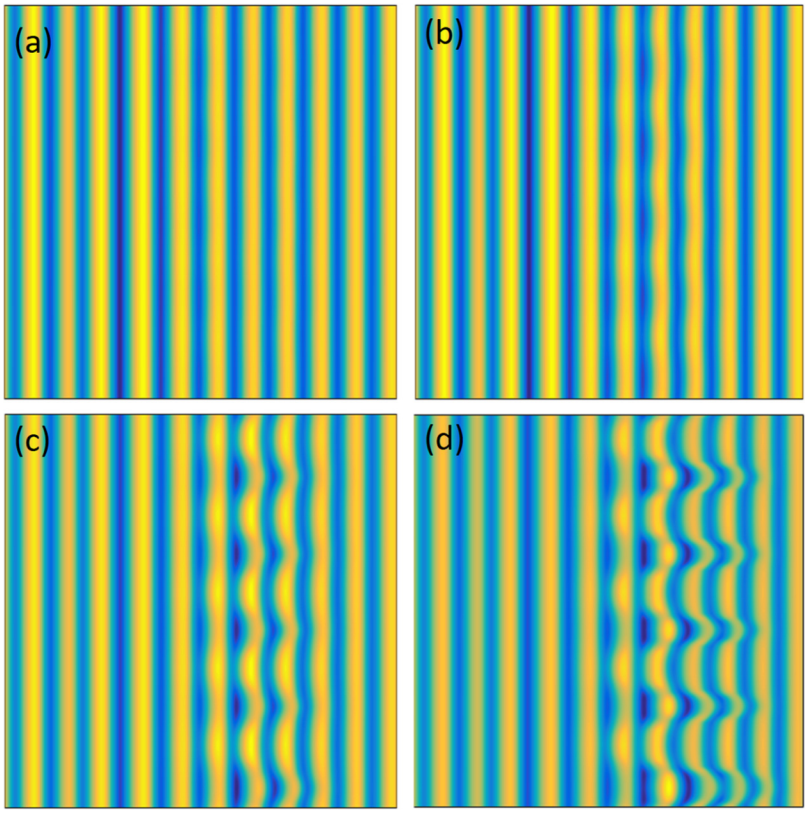

Fig. 8. Simulated ripples with different values of η, the parameter that controls the dependence of the lateral flux on the ripple height. (a) $\eta = 0.2$, (b) $\eta = 0.5$, (c) $\eta = 0.8$, (d) $\eta = 1$.

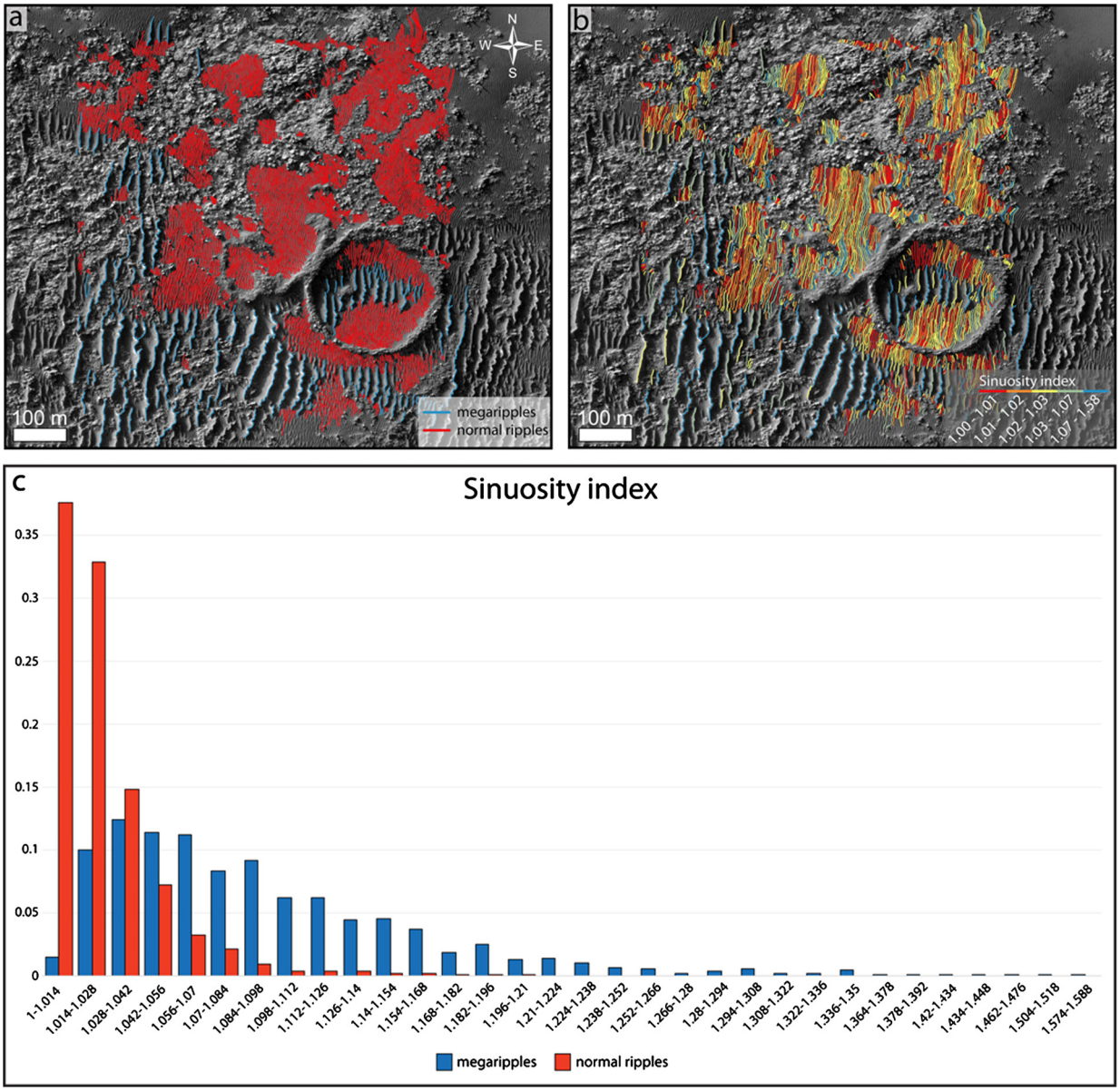

Fig. 9. (a) Two ripple classes, normal ripples and megaripples, are distinguished by means of the different wavelengths. (b) Sinuosity index derived for the two ripple classes (see also Supplementary Figs. S7 and S8). HiRISE image ESP_034801_1300, NASA/JPL/U of A. (c) Sinuosity index distribution for normal ripples and megaripples.

a smaller lateral flux than finer grains, and small random differences or perturbations in height along the crest can thus grow over time and lead to differential migration rates of different segments along the crest. Such random perturbations can be the result of wind variability in direction, streamers or small accumulations of coarse sand. This process enhances the instability since the translation speed of the ripple inversely scales with the ripple height. Thus, a ripple with a non-uniform height and small lateral flux is transversely unstable.

Recently, it was shown that megaripples can be interpreted as small dunes or reptation dunes dominated by the short distance transport of coarse grains (Lämmel et al., 2018). It was suggested that their morphometry is better described by dune characteristics, e.g., using the megaripple base length instead of the conventional wavelength (crest to crest distance). Thus, if megaripples behave like dunes, they are laterally unstable in the same manner as transverse dunes, and one isolated megaripple will eventually break into a chain of barchans (Parteli et al., 2011; Lämmel et al., 2018; Fig. S9). The reptation dune interpretation explains why, under conditions of low coarse sand supply, megaripples are much less regularly spaced and aligned than normal ripples and form mini-barchan structures (Fig. 1b), analogous to the formation of isolated barchans in environments with low sand supply. But as we noted above, the details of the processes in dunes and in megaripples are different despite their similar structures—chiefly gravitational sand flux in sand dunes versus the splash of coarse grains and differential sorting in megaripples. The model of Lämmel et al. (2018) can be considered as a starting point for a deeper understanding of the sorting mechanism, such as the mutual feedback between the evolution of topography and the lateral grain sorting. The current study moves one step further in understanding the lateral sorting and its impact on the morphology of megaripples, namely, the transverse instability. We show for the first time that in addition to the along-wind sorting that was previously studied (e.g. Sharp, 1963; Yizhaq et al., 2009; Qian et al., 2012), there is a cross-wind sorting that correlates with the megaripples' height. We do not have a full physical explanation as to why the lateral flux is smaller for coarse particles. One possi-

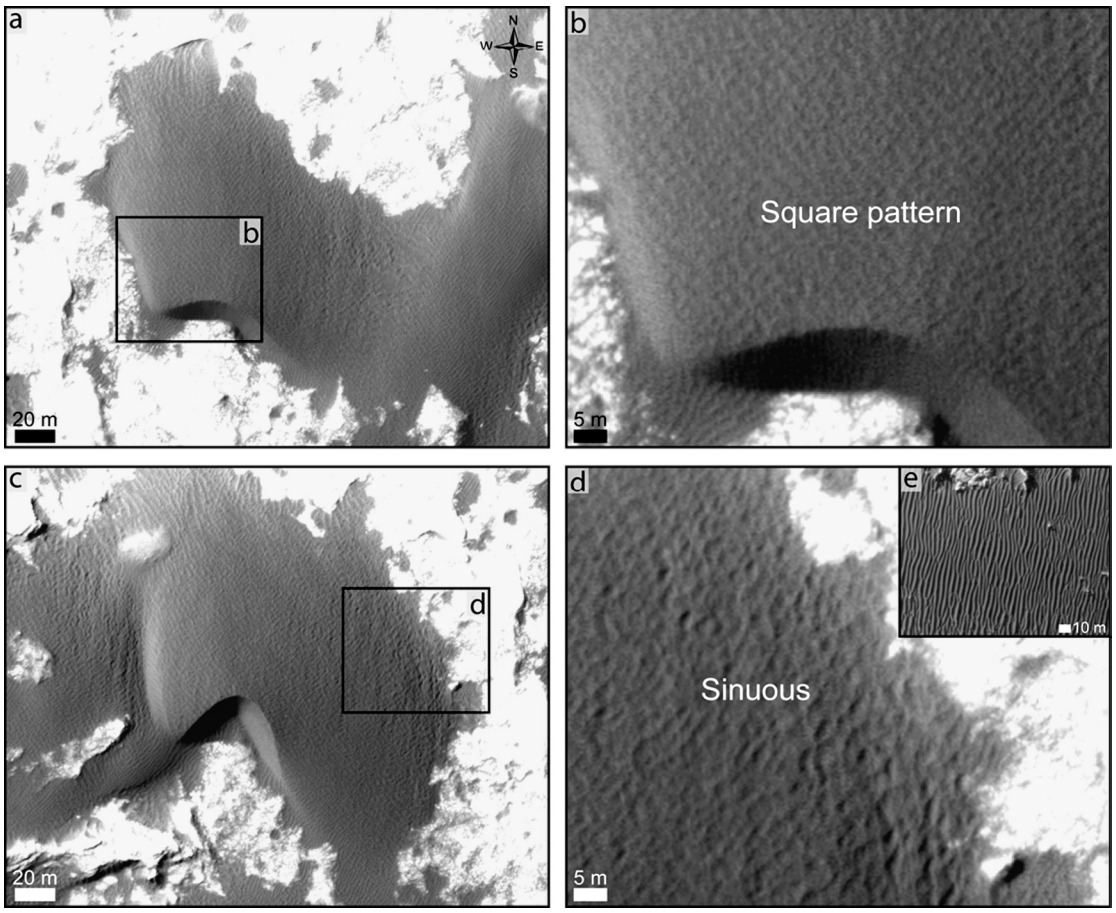

Fig. 10. Square patterned and sinuous ripples in the MSL Curiosity landing site as seen by the HiRISE camera (PSP_009294_1750, NASA/JPL/U of A). For the Curiosity's perspective, refer to Fig. 1c in Lapotre et al. (2016) and Fig. 4 in Ewing et al. (2017). Note the differences between the planar view in those figures and the examples studied in this work (inset e).

ble explanation is the effect of wind drag on the coarse grains. In order to account for small megaripples in their model, Manukyan and Prigozhin (2009) added a wind drag that acts mostly on coarse particles. The grains are dislodged by the saltation strikes and make a short jump, after which they roll upon the surface, not only under gravity but also due to the wind drag. They assumed that because the wind velocity quickly increases from zero with the distance from the bed (see Fig. 2.15 in Kok et al., 2012), the drag acts mostly on coarse grains. Although they are heavier, they are more exposed to a stronger wind. Following this line of explanation, for fine grains, the drag is unimportant, and their lateral flux mostly comes from the splash. For the coarse grains, the splash is tiny, whereas the drag is much more important, and it acts efficiently only in the wind direction. So for a significant surface concentration of coarse grains, the total sand flux should be more wind-oriented, in agreement with the wind tunnel experiments.

In contrast to megaripples, well-sorted normal ripples are composed of fine particles without an armoring layer and remain 2D bedforms, as height perturbations along the crest are rapidly dissipated by the lateral sand flux and by the direct entrainment of sand from the crest. Thus, in this case, the ripple crest will tend to be uniform in height and, consequently, straight in the planar view.

This mechanism will work to increase megaripples' sinuosity over time as long as the wind is below the saltation threshold of the coarse particles (Yizhaq and Katra, 2015). Above this threshold, the higher segments along the crest will be eroded due to local enhancement of the wind shear stress (Bar et al., 2016), and consequently, the sinuosity will decrease. In addition, strong storms can erode the armoring layer and flatten the megaripples (Isenberg et al., 2011). Another mechanism that can change the simple scheme is interactions between adjacent megaripples. Similar to what occurs in sand dunes (Kocurek et al., 2010; Ewing and Kocurek, 2010), these interactions will lead to a more complex planar geometry. In another scenario, a higher segment of one ripple can coalesce with a lower segment of a downwind ripple. The new segment will be higher and thus change the stability of the new ripple. It is also important to note that megaripples that develop on a slope will usually be straighter than megaripples on a plain, because of the lateral flux induced by gravity (Rubin, 2012; Fig. S10).

Based on our new understanding of the transverse instability for terrestrial megaripples, we can use the sinuosity index to discriminate between normal ripples and megaripples on Mars. The study area shows dunes oriented in different directions, but the study ripples have a constant N–S orientation, indicating that they are mainly shaped by unidirectional winds, likely blowing from the west to the east. This is important since multidirectional winds can form square (or cross-hatch) bedform patterns that can increase the ripples' sinuosity (e.g., Fig. S11 for terrestrial normal ripples and megaripples). The dark ripples in the Mars Science Laboratory (MSL) Curiosity Rover's landing site are an example of this situation (Bridges et al., 2017; Ewing et al., 2017; Lapotre et al., 2016; Silvestro et al., 2016) (Fig. 10a, b). In addition, it has been suggested that on Mars, large sinuous ripples can form without coarse grains and can be interpreted as fluid drag ripples (Ewing et al., 2017; Lapotre et al., 2016). However, the ripples investigated in this study are different from the ones visited by the Curiosity

Rover (Fig. 10). The 18-m-spaced megaripples investigated in this study have wavelengths in the range of small transverse aeolian ridges (TARs, Balme et al., 2008) and are more sinuous than the normal ripples nearby (Fig. 9).

According to previous studies, small TAR and megaripple wavelengths should not scale with the atmospheric density as suggested by the fluid drag theory (Ewing et al., 2017; Lapotre et al., 2016); thus, the higher sinuosity of these features should be due to the mechanism of grain size segregation described in this study. We thus give further support to the hypothesis that sees small TARs as megaripples (Hugenholtz et al., 2017; Lämmel et al., 2018). In addition, the lower wavelength ripples in the study area are straighter than the ones visited by Curiosity (Fig. 10b, c), and more similar to the El Dorado ripples visited by the NASA Mars Exploration Rover (MER) Spirit in the Gusev Crater and interpreted as normal impact ripples (Sullivan et al., 2008). Our results are thus in agreement with previous studies. Collectively, by combining fieldwork, wind tunnel experiments and image analysis from one Martian test site, we explain the mechanism behind the transverse instability of megaripples. This new mechanism highlights the importance of the grain size distribution in determining the morphological variability of the ripples and shows that sinuosity can be used to distinguish between different ripple types.

Acknowledgements

This work was supported by the German–Israeli Foundation for Scientific Research and Development (GIF Research Grant 1143-60.8/2011X), and by the National Science Foundation (Grant AGS-1358621 to J.F.K.). T. Elperin was supported by the Israel Science Foundation governed by the Israel Academy of Sciences (Grant No. 1210/15). S. Silvestro has been supported by the Agenzia Spaziale Italiana (ASI) through the ASI-CISAS agreement I/018/12/0: “DREAMS EDM Payload - ExoMars 2016”. The authors thank Leonid Prigozhin for his helpful discussions.

Appendix A. Supplementary material

Supplementary material related to this article can be found online at https://doi.org/10.1016/j.epsl.2019.01.025.

References

Anderson, R.S., 1987. A theoretical model for aeolian impact ripples. Sedimentology 34, 943–956. https://doi.org/10.1111/j.1365-3091.1987.tb00814.x.

Bagnold, R.A., 1941. The Physics of Blown Sand and Desert Dunes. Methuen, London.

Balme, M., Berman, D.C., Bourke, M.C., Zimbelman, J.R., 2008. Transverse Aeolian Ridges (TARs) on Mars. Geomorphology 101, 703–720.

Bar, N., Elperin, T., Katra, I., Yizhaq, H., 2016. Numerical study of shear stress distribution at sand ripple surface in wind tunnel flow. Aeolian Res. 21, 125–130.

Blott, S.J., Pye, K., 2001. GRADISTAT: a grain size distribution and statistics package for the analysis of unconsolidated sediments. Earth Surf. Process. Land. 26, 1237–1248.

Bourke, M.C., Lancaster, N., Fenton, L.K., Parteli, E.J.R., Zimbelman, J.R., Radebaugh, J., 2010. Extraterrestrial dunes: an introduction to the special issue on planetary dune systems. Geomorphology 121, 1–14. https://doi.org/10.1016/j.geomorph.2010.04.007.

Bridges, N.T., Ayoub, F., Leprince, S., Lucas, A., Mattson, S., 2012. Earth-like sand fluxes on Mars. Nature 485, 339–342. https://doi.org/10.1038/nature11022.

Bridges, N., Geissler, P., Silvestro, S., Banks, M., 2013. Bedform migration on Mars: current results and future plans. Aeolian Res. 9, 133–151. https://doi.org/10.1016/j.aeolia.2013.02.004.

Bridges, N.T., Sullivan, R., Newman, C.E., Navarro, S., van Beek, J., Ewing, R.C., Ayoub, F., Silvestro, S., Gasnault, O., Le Mouélic, S., Lapotre, M.G.A., Rapin, W., 2017. Martian aeolian activity at the Bagnold Dunes, Gale Crater: the view from the surface and orbit. J. Geophys. Res., Planets 122, 2077–2110. https://doi.org/10.1029/2006JE002825.

Cardinale, M., Silvestro, S., Vaz, D.A., Michaels, T., Bourke, M.C., Komatsu, G., Marinangeli, L., 2016. Present-day aeolian activity in Herschel Crater, Mars. Icarus 265, 139–148. https://doi.org/10.1016/j.icarus.2015.10.022.

de Silva, S.L., Spagnuolo, M.G., Bridges, N.T., Zimbelman, J.R., 2013. Gravel-mantled megaripples of the Argentinean Puna: a model for their origin and growth with implications for Mars. Geol. Soc. Am. Bull. 125, 1912–1929. https://doi.org/10.1130/B30916.1.

Durán, O., Claudin, P., Andreotti, B., 2014. Direct numerical simulations of aeolian sand ripples. Proc. Natl. Acad. Sci. USA 111 (44), 15665–15668.

Ewing, R.C., Kocurek, G., 2010. Aeolian dune interactions and dunefield pattern formation: White Sands Dune Field, New Mexico. Sedimentology 57, 1199–1219.

Ewing, R.C., Lapotre, M.G.A., Lewis, K.W., Day, M., Stein, N., Rubin, D.M., Sullivan, R., Banham, S., Lamb, M.P., Bridges, N.T., Gupta, S., Fischer, W.W., 2017. Sedimentary processes of the Bagnold Dunes: implications for the eolian rock record of Mars. J. Geophys. Res., Planets 122, 1–30. https://doi.org/10.1002/2017JE005324.

Foroutan, M., Zimbelman, J.R., 2016. Mega-ripples in Iran: a new analog for transverse aeolian ridges on Mars. Icarus 274, 99–105.

Gillies, J.A., Nickling, W.G., Tilson, M., Furtak-Cole, E., 2012. Wind-formed gravel bed forms, Wright Valley, Antarctica. J. Geophys. Res. 117, F04017. https://doi.org/10.1029/2012JF002378.

Hardisty, R.J.S., Whitehouse, J., 1988. Evidence for a new sand transport process from experiments on Saharan dunes. Nature 332, 532–534.

Hugenholtz, C.H., Barchyn, T.E., Boulding, A., 2017. Morphology of transverse aeolian ridges (TARs) on Mars from a large sample: further evidence of a megaripple origin? Icarus 286, 193–201. https://doi.org/10.1016/j.icarus.2016.10.015.

Isenberg, O., Yizhaq, H., Tsoar, H., Wenkart, R., Karnieli, A., Kok, J., Katra, I., 2011. Megaripple flattening due to strong winds. Geomorphology 131, 69–84.

Katra, I., Yizhaq, H., Kok, J., 2014. Mechanisms limiting the growth of aeolian megaripples. Geophys. Res. Lett. 41 (3), 858–865.

Katra, I., Yizhaq, H., 2017. Intensity and degree of segregation in bimodal and multimodal grain size distributions. Aeolian Res. 27, 23–34.

Kocurek, G., Ewing, R.C., Mohrig, D., 2010. How do bedform patterns arise? New views on the role of bedform interactions within a set of boundary conditions. Earth Surf. Process. Landf. 35, 51–63.

Kok, J.F., Parteli, E.J.R., Michaels, T., Bou Karam, D., 2012. The physics of wind-blown sand and dust. Rep. Prog. Phys. 75, 106901.

Lämmel, M., Meiwald, A., Yizhaq, H., Tsoar, H., Katra, I., Kroy, K., 2018. Aeolian sand sorting and megaripple formation. Nat. Phys. 14, 759–765. https://doi.org/10.1038/s41567-018-0106-z.

Lapotre, M.G.A., Ewing, R.C., Lamb, M.P., Fischer, W.W., Grotzinger, J.P., Rubin, D.M., Lewis, K.W., Ballard, M.J., Day, M., Gupta, S., Banham, S.G., Bridges, N.T., Marais, D.J. Des, Fraeman, A.A., Grant, J.A., Herkenhoff, K.E., Ming, D.W., Mischna, M.A., Rice, M.S., Sumner, D.A., Vasavada, A.R., Yingst, R.A., 2016. Large wind ripples on Mars: a record of atmospheric evolution. Science 353, 55–58. https://doi.org/10.1126/science.aaf3206.

Liu, Z.Y.C., Zimbelman, J.R., 2015. Recent near-surface wind directions inferred from mapping sand ripples on Martian dunes. Icarus 261, 169–181.

Manukyan, E., Prigozhin, L., 2009. Formation of aeolian ripples and sand sorting. Phys. Rev. E 79 (3), 031303. https://doi.org/10.1103/PhysRevE.79.031303.

McKenna Neuman, C., Bédard, O., 2016. A wind tunnel investigation of impact ripple formation in sands of varied texture. Earth Surf. Process. Landf. 42, 749–762.

Parteli, E.J.R., Andrade, J.S., Herrmann, H.J., 2011. Transverse instability of dunes. Phys. Rev. Lett. 107, 188001.

Pye, K., Tsoar, H., 2009. Aeolian Sand and Sand Dunes. Springer-Verlag, Berlin, Heidelberg.

Qian, G., Dong, Z., Zhang, Z., Lou, W., Lu, J., 2012. Granule ripples in the Kumtagh Desert, China: morphology, grain size and influencing factors. Sedimentology 59, 1888–1901.

Rubin, D.M., 2006. Ripple effect: unforeseen applications of sand studies. Eos 87 (30), 293–297.

Rubin, D.M., 2012. A unifying model for planform straightness of ripples and dunes in air and water. Earth-Sci. Rev. 113, 176–185.

Schmerler, E., Katra, E., Kok, J.F., Tsoar, H., Yizhaq, H., 2016. Experimental and numerical study of Sharp’s shadow zone hypothesis on sand ripple wavelength. Aeolian Res. 22, 37–46.

Sharp, R.P., 1963. Wind ripples. J. Geol. 71, 617–636.

Silvestro, S., Vaz, D.A., Fenton, L.K., Geissler, P.E., 2011. Active aeolian processes on Mars: a regional study in Arabia and Meridiani Terrae. Geophys. Res. Lett. 38, L20201. https://doi.org/10.1029/2011GL048955.

Silvestro, S., Vaz, D.A., Yizhaq, H., Esposito, F., 2016. Dune-like dynamic of Martian Aeolian Large Ripples. Geophys. Res. Lett. 43, 8384–8389. https://doi.org/10.1002/2016GL070014.

Sullivan, R., Banfield, D., Bell III, J.F., et al., 2005. Aeolian processes at the Mars Exploration Rover Meridiani Planum landing site. Nature 436. https://doi.org/10.1038/nature03641.

Sullivan, R., Arvidson, R., Bell III, J.F., Gellert, R., Golombek, M., Greeley, R., Herkenhoff, K., Johnson, J., Thompson, S., Whelley, P., Wray, J., 2008. Wind-driven particle mobility on Mars: insights from Mars Exploration Rover observations at “El Dorado” and surroundings at Gusev Crater. J. Geophys. Res., Planets 113, 1–70. https://doi.org/10.1029/2008JE003101.

Sullivan, R., Kok, J.F., Yizhaq, H., Siminovich, A., Elperin, T., Katra, I., 2018. Low dynamic wind pressures on Mars allow a broad continuum of aeolian ripple sizes. In: X International Conference on Aeolian Research.

Vaz, D.A., Silvestro, S., Sarmento, P.T.K., Cardinale, M., 2017. Migrating meter-scale bedforms on Martian dark dunes: are terrestrial aeolian ripples good analogues? Aeolian Res. https://doi.org/10.1016/j.aeolia.2016.08.003.

Yizhaq, H., Balmforth, N.J., Provenzale, A., 2004. Blown by wind: nonlinear dynamics of aeolian sand ripples. Physica D 195, 207–228.

Yizhaq, H., Isenberg, O., Wenkart, R., Tsoar, H., Karnieli, A., 2009. Morphology and dynamics of aeolian mega-ripples in Nahal Kasuy, southern Israel. Isr. J. Earth-Sci. 57, 149–165.

Yizhaq, H., Katra, I., Isenberg, O., Tsoar, H., 2012a. Evolution of megaripples from a flat bed. Aeolian Res. 6, 1–12.

Yizhaq, H., Katra, I., Kok, J., Isenberg, O., 2012b. Transverse instability of megaripples. Geology 40, 459–462.

Yizhaq, H., Katra, I., 2015. Longevity of aeolian megaripples. Earth Planet. Sci. Lett. 422, 28–32.

Zimbelman, J.R., Irwin III, R.P., Williams, S.H., Bunch, F., Valdez, A., Stevens, S., 2009. The rate of granule ripple movement on Earth and Mars. Icarus 203, 71–76.

Zimbelman, J.R., 2010. Transverse Aeolian Ridges on Mars: first results from HiRISE images. Geomorphology 121, 22–29.

Zimbelman, J.R., Bourke, M.C., Lorenz, R.D., 2013. Recent developments in planetary Aeolian studies and their terrestrial analogs. Aeolian Res. 11, 109–126.